CHARACTERIZATION OF THE FLOW OVER PERIODIC HILLS WITH ADVANCED MEASUREMENT AND EVALUATION TECHNIQUES

Christian Cierpka, Sven Scharnowski, Christian J. Kähler
Institute of Fluid Mechanics and Aerodynamics
Bundeswehr University Munich, Werner-Heisenberg-Weg 39, 85577 Neubiberg, Germany
christian.cierpka@unibw.de

Michael Manhart
Institute of Hydrodynamics
Technical University Munich, Arcisstr. 21, 80333 München, Germany
m.manhart@bv.tum.de

ABSTRACT

Due to the complex nature of turbulence, the simulation of turbulent flows is still challenging and numerical models have to be further improved. For the validation of these numerical flow simulation methods, reliable experimental data is necessary. A typical test case is the flow over periodic hills. The numerical prediction is difficult, since flow separation and reattachment are not fixed in space and time due to the smooth geometry (Temmerman *et al.*, 2003; Fröhlich *et al.*, 2005). Furthermore, the separated and fully three-dimensional flow from the previous hill impinges on the next hill, which results in very complex flow features. With the increasing computer performance available, it becomes possible to examine larger Reynolds numbers with DNS and LES. Typical grid sizes are in the order of several (3-10) Kolmogorov length scales η for LES and approach η for DNS (Breuer *et al.*, 2009). The resolution of currently available measurements is in the order of 30 η (Re = 8,000) and above which is not sufficient to resolve the large gradients in the shear layer at the hill crest. Even more severe, the contribution of the small eddies is averaged over a region associated with the measurement resolution. Thus an important part of the turbulent energy cannot be measured and is lost for the validation of turbulence models. Since these models are supposed to simulate the contribution of these small eddies it is of inherent interest to increase the resolution in the experiment. The aim of the current measurement campaign was therefore to increases the spatial resolution in order to provide a new data set for the validation of numerical tools.

Experimental setup and data evaluation

The particle image velocimetry experiments were performed in a geostatic driven water tunnel at TU Munich. The height h of the hills is 50 mm and the spacing between them, i.e. the periodicity, is $9h$. The channel had a total cross section of $3.035h \cdot 18h$. In order to produce a periodic flow, 10 hills were arranged in a row and the measurements were performed at the seventh hill. A detailed description of the setup can be found in Rapp & Manhart (2011). The main motivation for the current measurements was to obtain highly spatial and temporal resolved data to investigate the dynamic flow phenomena but also to characterize the statistics and flow features close to the wall, which could not be resolved in previous experiments due to the limited resolution of the techniques applied. To be able to relate the large structures that impinge on the uphill region with events in the wake flow of the hill, the measurement domain was centered around the hill. The coordinate system was also centered in x-direction at the hill top and at the bottom wall in the y-direction to allow for a comparison with the literature (Fröhlich *et al.*, 2005; Breuer *et al.*, 2009; Rapp & Manhart, 2011). The Reynolds number based on the averaged velocity above the hill crest, in the middle of the channel, u_b and the hill height was $Re = u_b h/\nu = 0.8 \cdot 10^4$ and $Re = 3.3 \cdot 10^4$.

It is useful to define an integral time scale t_{ref} for the following investigation. This reference time referrers to the time, required by an event or structure to travel with the mean velocity over the hill crest u_b through one periodic part of the channel, i.e. $9h$, and is also often denoted as 'flow through time' $t_{ref} = 9h/u_b$. This reference time is $t_{ref} = 2.63$ s for Re = 8,000 and $t_{ref} = 0.64$ s for Re = 33,000.

For the spatial resolution, the Kolmogorov length scale η can be estimated by taking the value of Breuer *et al.* (2009) obtained for DNS data at $Re = 5,600$ and scaling it with $Re^{3/4}$. This results in a mean Kolmogorov length scale of $\eta_{Re=8,000} \approx 100\mu m$ and $\eta_{Re=33,000} \approx 35\mu m$. In order to capture all relevant scales in space and time, two subsets of measurements were performed.

First, the whole flow field was sampled with 500 Hz for the lower Reynolds number and 2000 Hz for the higher Reynolds number using two Phantom V12 high-speed cameras. Standard window correlation-based data evaluation with a final interrogation window size of 16×16 pixels and 50% overlap were used to estimate the instanteneous flow fields. The motion of structures being transported through the whole period of $9h$ is therefore sampled with approximately 1,300 instantaneous velocity fields for both Reynolds numbers. The measurements were repeated four times, resulting in total measurement times of approximately 4·11 s = $16.7 \cdot t_{ref}$ and 4·3 s = $18.6 \cdot t_{ref}$, respectively.

Second, in order to achieve a reliable estimation of the turbulence statistics, the experiment was repeated using a scientific CMOS camera with a larger sensor (2560×2160 pixel) and small pixel size ($6.5\times6.5\mu$m^2). 22,000 double frame images were acquired with 5 Hz resulting in a total measurement time of 1.2 hours for each Reynolds number. Instantaneous velocity fields were again obtained by standard window correlation-based image evaluation with a final interrogation window size of 16×16 pixels and 50% overlap. However, this resolution is not sufficient to examine the high velocity gradients in the shear layer. To increase the spatial resolution for the mean values the single-pixel ensemble-correlation was used to estimate the mean flow fields (Kähler *et al.*, 2006). This technique provides a velocity vector at each pixel location. Since the final resolution, i.e. the distance of independent velocity vectors, does strongly depend on the particle image size (Kähler *et al.*, 2012), the final resolution is 0.45 mm. The velocity field is therefore 5 times better resolved than in previous measurements reported by Rapp & Manhart (2011). For Re = 8,000 this results in a spatial resolution of $4.4{\cdot}\eta$ and to $12.7{\cdot}\eta$ for Re = 33,000, which is comparable to the direct numerical simulations performed by Breuer *et al.* (2009). Scharnowski *et al.* (2012) developed a method to determine the Reynolds stresses with the same spatial resolution and recently extended the technique to higher order moments.

Turbulent statistics

The large variance of structures and events on different time scales can be seen in the instantaneous flow fields as shown in Fig. 1 for the stream-wise velocity component. Due to the confinement of the channel the flow accelerates towards the hill. Behind the hill a separated region can be clearly seen in the instantaneous velocity fields with a very irregular interface towards the free stream region. The large structure in front of the hill moved slightly downstream and decreased considerably in size during the time between the two flow fields $t = 0.15 \cdot t_{\text{ref}}$.

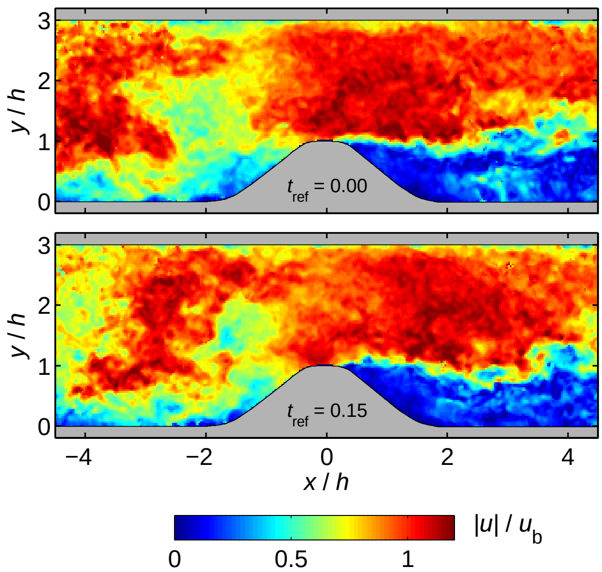

Figure 1. Instantaneous velocity fields for Re = 8,000.

For a detailed analysis it is important to make sure that the mean values for this highly turbulent flow reached statistical convergence. As a criterion for convergence a deviation of the mean value of 0.05 pixel was chosen for the mean displacement and 0.01 pixel for the turbulence intensity. Since the sampling rate for the 22,000 instantaneous velocity fields was the same for both Reynolds numbers, a total measurement time of $T = 1{,}680 \cdot t_{\text{ref}}$ was achieved for Re = 8,000 and $T = 6{,}840 \cdot t_{\text{ref}}$ for Re = 33,000. Therefore, the convergence of the mean values within the total measurement time for the lower Reynolds number are more critical. To prove the statistical convergence, the evolution of the mean values for the stream-wise velocity $\langle u \rangle / u_{\text{b}}$ and the turbulence level Tu/u_{b} vs. t/t_{ref} is shown in Fig. 2 for three different wall-normal positions at $x/h = 1.8$. As expected the time to reach the convergence criteria for the turbulence level is much higher compared to the time neccessary for the velocity distribution. However, the time span also differers considerably for the different positions within the flow field.

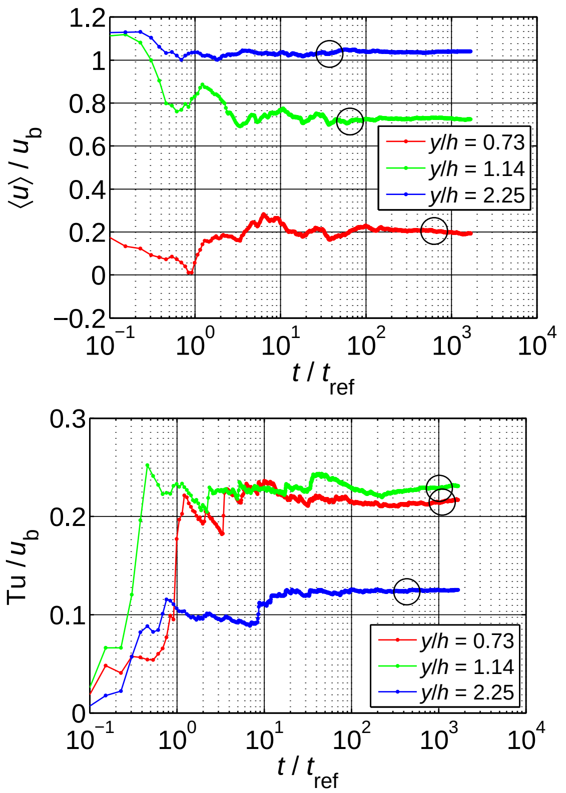

Figure 2. Evolution of the mean value for the stream-wise velocity u/u_{b} (top) and the turbulence level Tu/u_{b} vs. t/t_{ref} for three different wall-normal positions at $x/h = 1.8$.

The spatial distribution of the time necessary to reach the convergence criteria of the stream-wise mean velocity $\langle u \rangle$ and the turbulence level Tu for Re = 8,000 is shown in Fig 3. The three different positions are indicated as circles. As can be seen in the figure, the convergence for the upper half of the channel can be reached for fairly low time spans. A much larger time span is necessary in the region of the developing shear layer where the flow shows higher turbulence and vortex interaction. However, in the uphill region a large time span is also required due to the impinging of the vortices on the hill. These findings are especially interesting for numerical simulations where it is usually difficult to acquire as many time steps for reliable mean values.

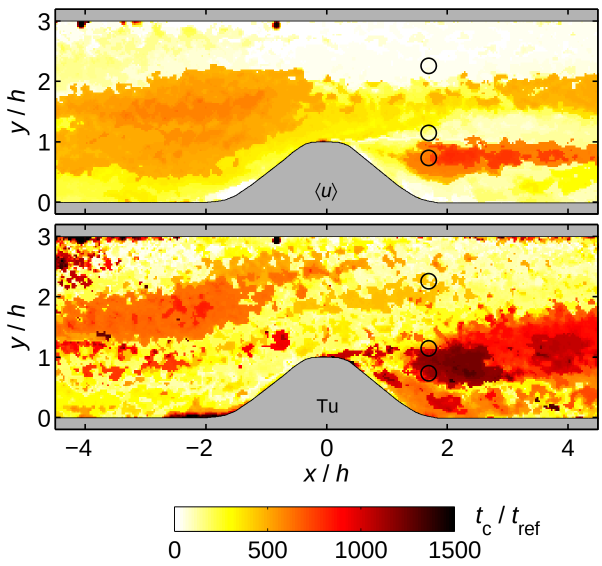

Figure 3. Spatial distribution of the duration to reach the convergence criteria of the stream-wise mean velocity $\langle u \rangle$ and the turbulence level Tu for Re = 8,000. The circles mark the convergence time.

In Fig. 4 the absolute value of the time averaged velocity field in stream-wise direction, obtained by single-pixel ensemble-correlation analysis is shown. The acceleration over the hill can be clearly seen. At the hill top a narrow shear layer develops and starts to detach from the hill at x/h = 0.23 for Re = 8,000. Due to the higher momentum the flow follows the contour of the hill and separates further downstream at x/h = 0.31 for the larger Reynolds number. Downstream of the hill a recirculation zone, highlighted by the stream lines, develops. The center of this recirculation zone is approximately at the same stream-wise position at $x/h \approx 2.1$ for both Reynolds number. For the lower Reynolds number the length of the recirculation zone is $4.29 \cdot x/h$ and therefore about 15% larger than for the higher Reynolds number. The values are in good agreement with Rapp & Manhart (2011). The heigth of the recirculation zone and therefore also the wall-normal position of the center also differs with y/h = 0.51 for Re = 8,000 and y/h = 0.46 for Re = 33,000. The main experimental parameters are summarized in Tab. 1.

In order to compare the flow at both Reynold numbers, profiles of the mean stream-wise velocity, the turbulence intensity and the Reynolds shear stresses are shown in Fig. 5. The high spatial resolution of the measurements allows for the determination of the large gradient of the velocity overshoot at the hill top as can clearly be seen in the upper plot. The velocity overshoot at x/h = 0.05 is about $0.11 \cdot u_\mathrm{b}$ for Re = 8,000 and $0.18 \cdot u_\mathrm{b}$ for Re = 33,000 in the time averaged sense. Due to the confinement of the flow the velocity in the upper half of the channel is slightly larger than the bulk velocity for Re = 8,000 which is not the case for the higher Reynolds number. For the higher Reynolds number a larger momentum exchange is expected, which can clearly be seen at $x/h = 1$ for instance, where the momentum deficit in the recirculation zone is already substantially smaller than for the lower Reynolds number. However, the

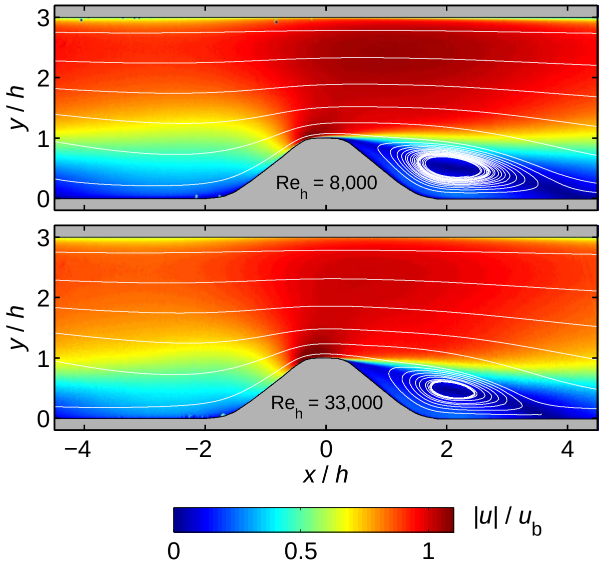

Figure 4. Spatial distribution of the mean velocity's absolute value and characteristic streamlines for Re $= 8{,}000$ (top) and Re $= 33{,}000$ (bottom).

flow finally reattaches in a time averaged sense. Due to the high spatial resolution the small differences for the different Reynolds numbers can clearly be measured, as for example the very thin remaining region of reversed flow for the lower Reynolds number seen in the profile at x/h = 4. In general, the momentum transfer from the free stream to the recirculation zone is lower for the lower Reynolds number and thus the profiles in the upper half of the channel show higher velocities compared to Re = 33,000 and vice versa in the lower half of the channel.

For the validation of numerical methods the Reynolds stresses are of particular interest, as they are determined from turbulence models, which are always uncertain, in numerical flow simulations. As already mentioned, the Reynolds stresses were directly determined from the correlation functions obtained by the single-pixel ensemble-correlation and thus a final resolution of 0.45 mm in each direction was achieved.

The profiles for the turbulence intensity Tu $= \sqrt{\left(\langle u'^2 \rangle + \langle v'^2 \rangle\right)/2}$ show the largest values in the evolving shear layer at the hill top. With the wall-normal growth of this shear layer, the turbulence profiles become smoother. However, the peak at $y/h \approx 0.75$ can still be seen for the flow, impinging on the hill at $x/h = -3 \ldots -2$. Due to the confinement and the acceleration of the flow by the geometry of the hill, the turbulence levels decrease strongly in the uphill region.

The Reynolds shear stresses for both Reynolds numbers are shown in Fig. 5. It is obvious that the Reynolds shear stresses for the larger Reynolds number reach a much higher level than for Re = 8,000 as expected. The difference is particularly pronounced within the recirculation region. Also the wall-normal position of the maximum is lower for the higher Reynolds number. This effect is due to the larger momentum exchange which effects the position of the shear layer. The height of the layer with high Reynolds shear stresses is also much smaller for the higher Reynolds number. However, the highest values are to be observed in the thin shear layer evolving from the hill top and smooth out for further downstream positions especially when the flow starts to accelerate due to the next hill.

In conclusion, the single-pixel ensemble-correlation provides the necessary spatial resolution to characterize the flow in a time averaged sense and to elaborate on the evolution of the large scale structures and regions of high phenomenological relevance.

Table 1. Main experimental parameters.

	case 1	case 2
$\mathrm{Re_h}$	≈8,000	≈33,000
t_{ref} in s	2.62	0.645
T/t_{ref}	1,680	6,840
u_{b} in m/s	0.171	0.698
$\langle\vec{u}\rangle_{\max}/u_{\mathrm{b}}$	1.106 ± 0.003	1.178 ± 0.004
at x/h	-0.29 ± 0.02	-0.33 ± 0.02
at y/h	1.03 ± 0.02	0.99 ± 0.02
flow separation		
at x/h	0.23 ± 0.05	0.31 ± 0.05
recirculation center		
at x/h	2.07 ± 0.03	2.09 ± 0.04
at y/h	0.51 ± 0.01	0.46 ± 0.02
x_{r}/h	4.29 ± 0.02	3.73 ± 0.03

Flow dynamics

To characterize the dynamics of the whole flow field a POD decomposition was undertaken. The POD modes (not shown) of the fluctuating velocity fields can be interpreted as regions of high momentum exchange (Cierpka *et al.*, 2010). The distribution of the modes revealed, that a very dominant momentum exchange takes place in the region where the shear layer from the previous hill impinges on the uphill region of the next hill. The second most dominant mode indicated a very large region at the downstream position which is much larger than the recirculation zone. The momentum exchange in the shear layer itself shows up in higher modes, i.e. it represents lower energetic events for the flow. To evaluate the time scales in the different regions a frequency analysis for the whole flow field was performed. Since the flow is highly turbulent very broad spectra were observed. However, no distinct clear peak for, e.g. a dominant vortex shedding frequency or the Kelvin-Helmholtz instabilities, could be identified.

The identification of the vortical structures can provide significant information on the overall evolution of the flow since these structures are related to mixing and momentum transfer. To distinguish between vorticity generated by shear and vorticity belonging to a vortical structure the D_2-criteria has been proved to be a suitable filter (Vollmers, 2001). The vortex identification is now based on the swirling strength $s = \max(0; D_2) \cdot \mathrm{sign}\omega$, which is the product of the negative part of the discriminant of the velocity gradient matrix and the sign of the vorticity to allow for the determination of the rotation direction. The swirling strength distribution of all vector fields was used to detect the vortices. A cross-correlation between the swirling strength and a set of Gaussian distributions with varying diameters was computed following similar approaches as described by Schram *et al.* (2004) and Cierpka *et al.* (2010). The position of the correlation peak gives an estimate of the vortex position and the height determines the quality of the correspondence between the vortical structure and the Gaussian and allows for size estimation. However, since deformed vortices are also likely to appear, the final size estimation was done using a parametric fit with a Gaussian distribution. Fit parameters were both axes and the orientation angle (Scharnowski & Kähler, 2011). In total, about 5,000,000 vortices were detected with an average core size (major axis) of about $D = 0.09 \cdot h$ where smaller vortices are more likely to appear. However, large structures up to $D = 0.4 \cdot h$ were also identified. The spatial distribution of the vortical structures is shown in Fig. 6. The smallest structures with a mean diameter of $D < 0.07 \cdot h$ are presented at the top. As can be seen from the colors, these sizes are most likely to appear at the upper wall of the channel. The developing shear layer is also clearly indicated by the higher values in the region where the vortices are produced ($0 < x/h < 2$). The vortices grow with downstream position in size and a second region of a more likely appearance of smaller structures is to be found at a region of $3 < x/h < 4$ which is supposed to be in a region where the larger vortices start to decay. In the middle section of Fig. 6 the distribution of structures with a size of $0.07 \cdot h < D < 0.1 \cdot h$ is shown. These structures appear with higher probability in the lower part of the channel, in front of the hill and in the region of the reattachment, but do not propagate into the recirculation zone. The largest structures $D > 0.1 \cdot h$, as shown in the bottom part of the same figure, do appear also in the recirculation zone as can clearly be seen in the figure.

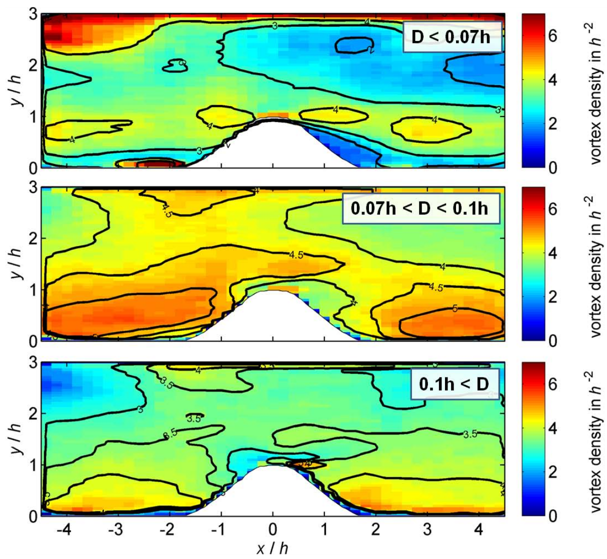

Figure 6. Spatial distribution of the vortex density for Re $= 8{,}000$ for structures with $D < 0.07 \cdot h$ (top), $0.07 \cdot h < D < 0.1 \cdot h$ (middle) and $0.1 \cdot h < D$ (bottom).

In Fig. 7 the two point correlation of the velocity in the stream-wise R_{uu} and wall-normal R_{vv} directions are shown for different locations within the flow field and Re = 33,000. The two–point correlation is the correlation of the vector at

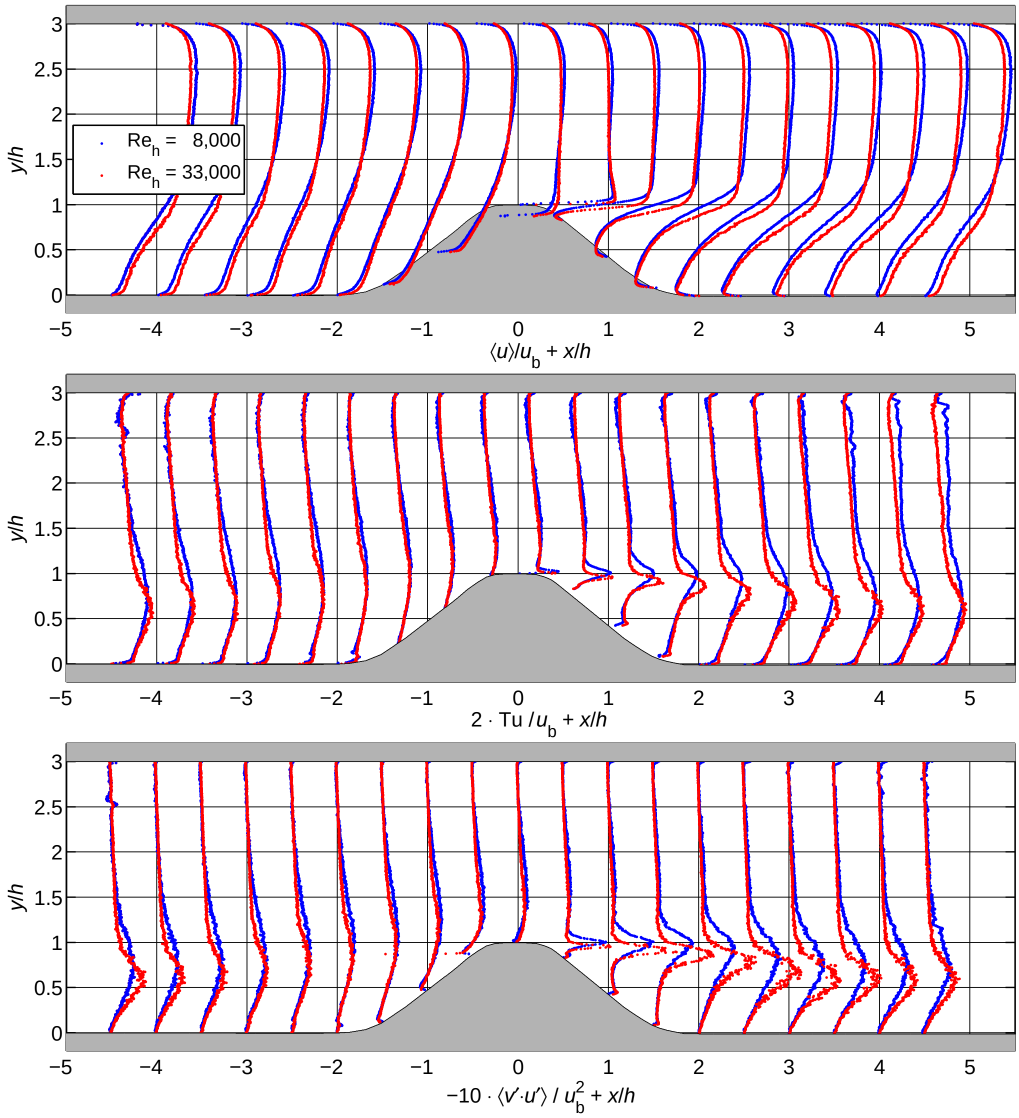

Figure 5. Profiles for the mean stream-wise velocity (top) , the turbulence intensity (middle) and the Reynolds shear stress (bottom) for Re = 8,000 (blue) and Re = 33,000 (red).

the point of interest (x_0, y_0) with all points within the field of view (x, y). The distribution can be interpreted as coherent length or size of typical structures or regions where the flow field is influenced by events occurring at the position of the '+' sign. In the upper part of the figure, the two point correlation for a position in the uphill region can be seen. The flow at this position is accelerated by the confinement of the channel. For both distributions, very large connected regions in front of the hill can be seen indicating large coherent structures. For R_{vv} a thin layer of a negative correlation is visible at the upstream side of the hill. This means that an upward motion at $x/h = -2.0$ and $y/h = 0.5$ is related to a downward motion on the hill surface. This region is probably caused by the splashing of vortices and also results in the negative shear stress distribution in that region, visible in Fig. 5 (bottom). The same phenomena can be observed for $x/h = -1.0$ and $y/h = 0.5$. For the correlation in the stream-wise direction R_{uu}, a large region of weak negative correlation is visible in the upper part of the channel indicating that a movement in the stream-wise direction at the wall causes a deceleration in the upper part of the channel and vice versa. Approximitelly at the hill top only positive correlation can be found caused by the maximum confinement which damps out almost all structures due to the strong acceleration. In the recirculation zone at $x/h = 2.0$ and $y/h = 0.5$ regions of positive and negative correlation are again visible indicating structures forming from the shear layer and merging and dissipating in that region.

Conclusion and outlook

The first examination of the mean velocity, turbulence levels and Reynolds stress distributions already indicated that with advanced measurement equipment and sophisticated evaluation techniques many new flow features can be resolved. The frequency analysis of the flow showed a very broad spectrum typical for highly turbulent flows. To further examine the dynamics and the momentum transfer in the flow, an analysis of the appearance and size of vortical structures, as well as two-point correlation, was used and can help for the understanding of the flow. This gives new insight into the complex flow phenomena and allows to prove the numerical predictions, which could not be val-

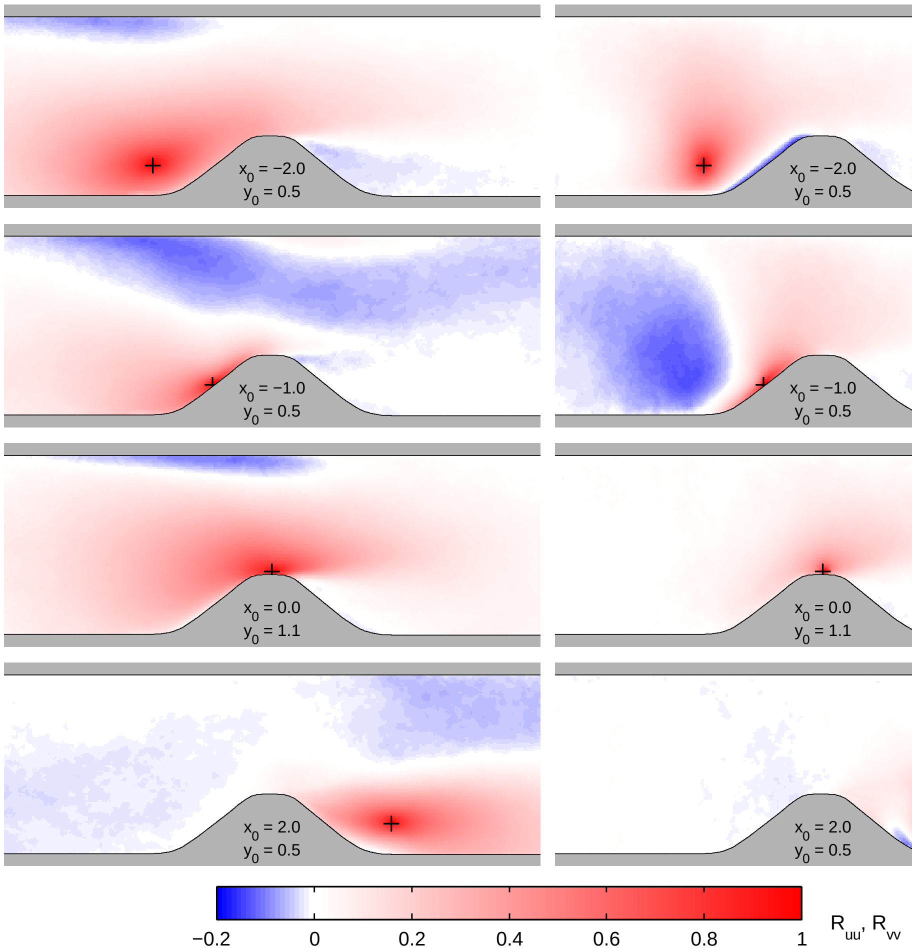

Figure 7. Spatial distribution of the two-point correlation of the horizontal (left) and vertical (right) velocity component for different locations, marked by the '+' signs for Re = 33,000.

idated in the past due to a lack in spatial resolution for experimental data.

Acknowledgments

The financial support from the European Community's Seventh Framework program (FP7/2007-2013) under grant agreement No. 265695 and from the German research foundation (DFG) under the individual grants program KA 1808/8 and Transregio 40 is gratefully acknowledged.

REFERENCES

Breuer, M., Peller, N., Rapp, C. & Manhart, M. 2009 Flow over periodic hills- Numerical and experimental study in a wide range of Reynolds numbers. *Comp Fluids* **38**, 433–457.

Cierpka, C., Weier, T. & Gerbeth, G. 2010 Synchronized force and particle image velocimetry measurements on a NACA 0015 in poststall under control of time periodic electromagnetic forcing. *Phys Fluids* **22**, 075109.

Fröhlich, J., Mellen, C.P., Rodi, W., Temmerman, L. & Leschziner, M.A. 2005 Highly resolved large-eddy simulation of separated flow in a channel with streamwise periodic constrictions. *J Fluid Mech* **526**, 9–66.

Kähler, C. J., Scharnowski, S. & Cierpka, C. 2012 On the resolution limit of digital particle image velocimetry. *Exp Fluids* **52**, 1629–1639.

Kähler, C. J., Scholz, U. & Ortmanns, J. 2006 Wall-shear-stress and near-wall turbulence measurements up to single pixel resolution by means of long-distance micro-PIV. *Exp Fluids* **41**, 327–341.

Rapp, C. & Manhart, M. 2011 Flow over periodic hills: an experimental study. *Exp Fluids* **51**, 247–269.

Scharnowski, S., Hain, R. & Kähler, C. J. 2012 Reynolds stress estimation up to single-pixel resolution using PIV-measurements. *Exp Fluids* **52**, 985–1002.

Scharnowski, S. & Kähler, C. J. 2011 Investigation of the wake dynamics of a generic space launcher at Ma = 0.7 by using high-repetition rate PIV. In *4th European Conference for Aerospace Sciences, Saint Petersburg, Russia, July 4-8*.

Schram, C., Rambaud, P. & Riethmuller, M. L. 2004 Wavelet based eddy structure eduction from a backward facing step flow investigated using particle image velocimetry. *Exp Fluids* **36**, 233–245.

Temmerman, L., Leschziner, M.A., Mellen, C.P. & Fröhlich, J. 2003 Investigation of wall-function approximations and subgrid-scale models in large eddy simulation of separated flow in a channel with streamwise periodic constrictions. *Int J Heat Fluid* **24**, 157–180.

Vollmers, H. 2001 Detection of vortices and quantitative evaluation of their main parameters from experimental velocity data. *Meas Scie Tech* **12**, 1199–1207.